ELSEVIER

Journal of Power Sources 4819 (2002) 1–6

JOURNAL OF POWER SOURCES

www.elsevier.com/locate/jpowsour

Magnesium silicide as a negative electrode material for lithium-ion batteries

G.A. Roberts*, E.J. Cairns, J.A. Reimer

Ernest Orlando Lawrence Berkeley National Laboratory, and Department of Chemical Engineering, University of California at Berkeley, Berkeley, CA 94720, USA

Abstract

Mg_2Si was synthesized by mechanically activated annealing and evaluated as a negative electrode material. A maximum discharge capacity of 830 mAh/g was observed by cycling over a wide voltage window of 5–650 mV versus Li, but capacity fade was rapid. Cycling over the range 50–225 mV versus Li produced a stable discharge capacity of approximately 100 mAh/g. X-ray diffraction (XRD) experiments showed that lithium insertion converts Mg_2Si into Li_2MgSi after lithium intercalation into Mg_2Si. Electrochemical evidence of Li–Si reactions indicated that the Li_2MgSi structure can be converted to binary lithium alloys with extensive charging. © 2002 Published by Elsevier Science B.V.

Keywords: Magnesium silicide; Mg_2Si; Anode materials; Lithium batteries

1. Introduction

Graphite is commonly used as a negative electrode material in lithium batteries, but higher capacity alternatives with lower irreversible capacities are being pursued. Several binary lithium alloys (e.g. Li–Al, Li–Si, and Li–Sn) have been investigated as possible replacements for graphite, but capacity retention during cycling is limited by large volume changes within the alloys [1]. Recent research on negative electrode materials has included intermetallic systems which may offer larger capacities than graphite and better cycling performances than binary alloys.

Magnesium silicide (Mg_2Si), the only intermetallic in the Mg–Si system, has several desirable features for a battery material. Lithium can be inserted into Mg and Si at room temperature, and both elements are naturally abundant, light-weight, and inexpensive. Pure Mg_2Si is difficult to prepare by conventional melting techniques because the melting points of magnesium and silicon differ by 760 °C, but Mg_2Si can be synthesized in a solid-state reaction by mechanical alloying.

Two studies with conflicting reaction schemes have demonstrated that Mg_2Si can reversibly store lithium at room temperature [2,3]. Kim et al. reported that lithium was intercalated into Mg_2Si. After the lithium intercalation limit was reached, they reported that the Mg_2Si structure was destroyed, forming binary Li–Mg and Li–Si alloys. As with the study by Anani and Huggins at 400 °C, [4] they did not observe any unique ternary phases. However, Moriga et al. proposed a two-step sequence that starts with the formation of a unique ternary phase, Li_2MgSi. This ternary phase is similar to a high temperature phase prepared non-electrochemically by Wengert et al. [5], Moriga et al. observed two potential plateaus during lithium insertion, and they concluded that the second plateau was due to lithium insertion into the magnesium that had been discharged from Mg_2Si to produce Li_2MgSi.

In this study, we present our efforts on the synthesis and electrochemical characterization of Mg_2Si. Mg_2Si was synthesized by mechanically activated annealing (mechanical alloying followed by a brief heat treatment). X-ray diffraction (XRD) was used to investigate structural changes during galvanostatic cycling.

2. Experimental

A planetary ball mill (Fritsch P-7 Planetary Mono Mill) was used to synthesize Mg_2Si from elemental powders. Mg (99.8% pure, 325 mesh) and Si (99.9% pure, 100 mesh) powders were obtained from Alfa Aesar. Milling was performed in a 45 ml stainless steel grinding bowl with an O-ring seal. Five grams of powder, five stainless steel balls of 0.375 in. diameter, and 1 ml of hexane were added to the bowl in an argon-filled glove box. Milling was performed at

* Corresponding author.
E-mail address: ejcairns@lbl.gov (G.A. Roberts).

0378-7753/02/$ – see front matter © 2002 Published by Elsevier Science B.V.
PII: S0378-7753(02)00207-0

a disc rotation speed of 400 rpm. Synthesis products were studied with an X-ray diffractometer (Siemens Diffraktometer D5000, Cu Kα radiation) and a particle-size analyzer (Beckman Coulter LS230).

Electrodes were prepared by drying an electrode slurry (75 wt.% active material, 15 wt.% acetylene black, and 10 wt.% polyvinylidene fluoride dissolved in *N*-methyl-2-pyrrolidine) on a copper foil at 120 °C under vacuum. Electrode discs with a 0.625 in. diameter and approximately 15 mg of active material were cut from the foil.

Cells were assembled with Swagelok union tube fittings and polypropylene ferrules in an argon-filled glove box. Separators were cut from Celgard 3401. Lithium foil was used as counter and reference electrodes. Merck Selectipur LP32 (1 M $LiPF_6$ in 2:1 dimethylene carbonate/ethylene carbonate) was used as the electrolyte. An Arbin battery testing system was used for galvanostatic cycling. All cells were cycled at 15 mA/g active material and 20 °C unless otherwise noted. Cycled electrodes were prepared for XRD measurements by covering them with Kapton tape in a glove box.

3. Results and discussions

3.1. Mg_2Si synthesis

XRD patterns of samples removed during synthesis are shown in Fig. 1. After 5 h of milling, only the starting materials were observed. After 20 h of milling, the starting materials still dominated the pattern, but a weak (2 2 0) Mg_2Si peak could be discerned at 40°. The weak peak at 45° was attributed to Fe_3Si contamination. The intensity of this peak was too weak to estimate the amount of the contaminant in the sample, but Niu and Lu have reported iron contamination in excess of 1 at.% after 30 h of milling under different milling conditions [6]. Contamination, which is expected when milling a hard material like silicon, could be reduced by using milling tools constructed from harder materials (e.g. hardened chrome steels).

The changes in relative intensities between Mg and Si during milling were dramatic. After 5 h of milling, the Mg (1 0 1) peak at 37° was stronger than the Si (1 1 1) peak at 29°. After 20 h of milling, the Si (1 1 1) peak was the strongest peak in the pattern. One possible cause could be cold-welding of magnesium to the grinding tools, which would lower the magnesium concentration in the powder. However, inspection of the grinding bowl revealed that the process control agent, hexane, successfully prevented significant cold-welding to the grinding tools. Another explanation is that silicon is the host phase and magnesium is the mobile phase. Diffusion of magnesium into the silicon host would explain the Mg intensity loss with increased milling.

Fig. 1c shows the XRD pattern for the sample prepared by mechanically activated annealing. The sampled was milled for 5 h and annealed at 600 °C in an argon atmosphere for 2 h. The heat treatment allowed for complete formation of Mg_2Si with small milling times. Residual magnesium and silicon were not detected in the diffraction pattern. Of course, the annealed product had much sharper diffraction lines than those shown in Fig. 1a and b because the heat treatment allowed for crystallite growth and relaxation of lattice strain that accumulated during milling.

The mechanically alloyed Mg_2Si particle size distribution is shown in Fig. 2. The lower limit for the particle size analyzer was 400 nm. On a volume percent basis, the mean particle size was 30.12 mm. On a per particle basis, the mean particle size was 0.96 mm.

3.2. Electrochemical results for Mg_2Si

Voltage profiles for the first two galvanostatic cycles for Mg_2Si cycled over 25–650 mV versus Li are shown in Fig. 3. For the first insertion, the lithium capacity at high potentials was attributed to the formation of a SEI layer. The large

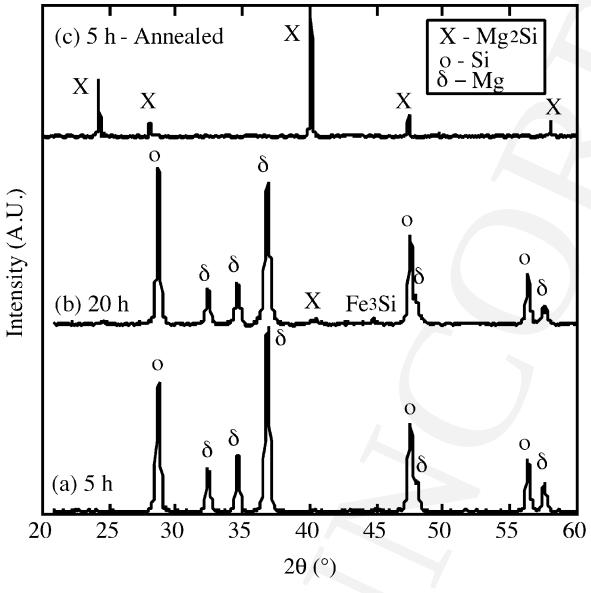

Fig. 1. XRD patterns for Mg_2Si synthesis milled for: (a) 5 h; (b) 20 h and (c) 5 h and heated to 600 °C.

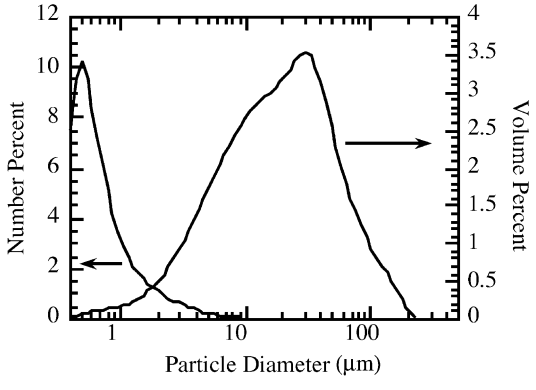

Fig. 2. Particle size distribution for mechanically alloyed Mg_2Si.

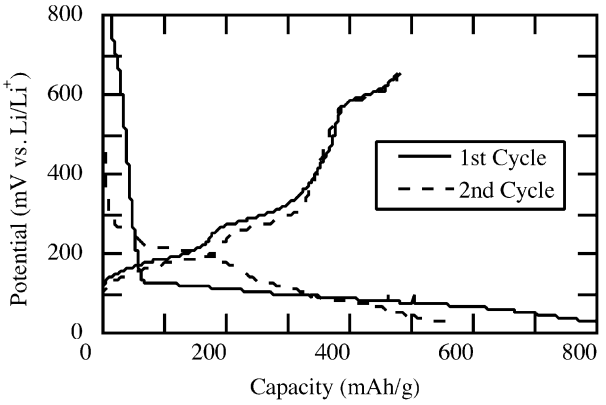

Fig. 3. Voltage profiles for Mg_2Si cycled between 25 and 650 mV vs. Li.

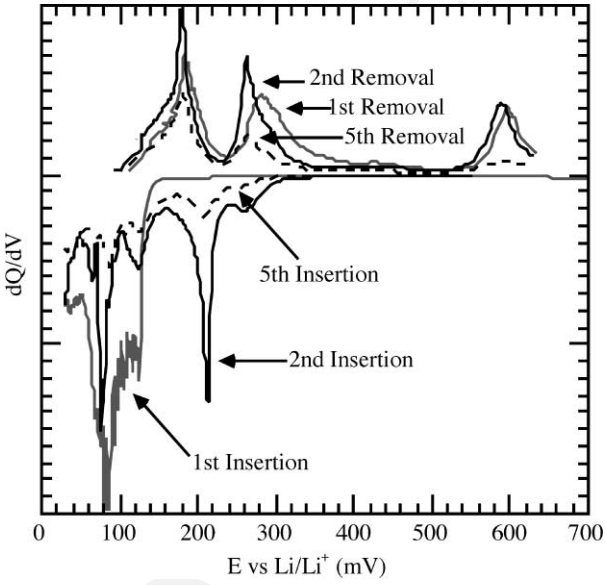

Fig. 4. DCPs for Mg_2Si cycled between 25 and 650 mV vs. Li.

irreversible capacity in the first cycle was due to the formation of the SEI and to reduction of surface oxides. The first insertion had larger overpotentials and fewer voltage plateaus than subsequent insertions. The absence of expected plateau features during cycling can indicate kinetically hindered reconstitution reactions. Unlike the insertion profiles, the features that were present for lithium removal in the second cycle were also present in the first cycle.

Fig. 4 shows the differential capacity plots (DCPs) for the first, second, and fifth cycles for Mg_2Si cycled over 25–650 mV versus Li. The differences between the potentials at the end of lithium insertion and the start of lithium removal were due to 0.5 h open-circuit pauses that allowed the potentials to drift towards equilibrium. For the first insertion, significant lithium insertion did not occur until the potential reached 120 mV versus Li. Overpotentials for the first lithium removal were larger than for the following cycles. After the material was activated during the first cycle, peak positions remained constant. This indicated that overpotentials were not increasing during cycling, so it does not appear that SEI layer thickening is a problem with Mg_2Si in this electrolyte. As seen from the fifth cycle, the fastest capacity fade occurred over the 600 mV region.

Cycle lives for Mg_2Si, cycled at 15 mA/g over several voltage windows, are shown in Fig. 5. Insertion to more negative potentials dramatically improved maximum discharge capacities, but the capacity fade rates also increased. The maximum discharge capacity that we observed was 830 mAh/g for the first cycle over a 5–650 mV window. The electrode that was cycled over a 100–650 mV window required several cycles to reach its maximum capacity. Insertion to 100 mV was barely sufficient to reach potentials where significant insertion started to occur (approximately 120 mV versus Li as shown in Fig. 4), so this electrode needed several cycles to activate. Stable capacities of

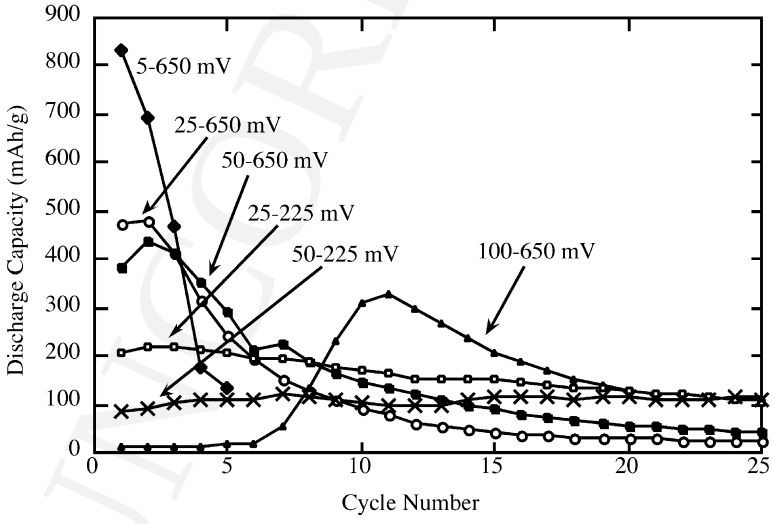

Fig. 5. Cycle lives for Mg_2Si cycled over various voltage windows.

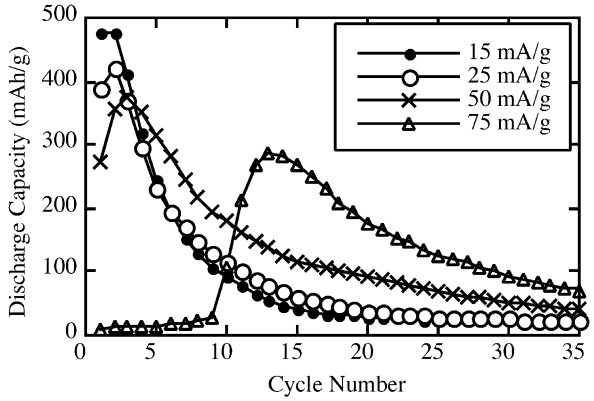

Fig. 6. Cycle lives for Mg_2Si cycled over 25–650 mV vs. Li at various current densities.

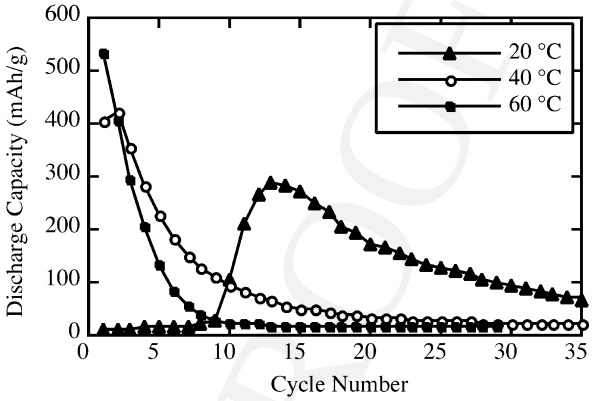

Fig. 8. Cycle lives for Mg_2Si cycled over 25–650 mV at various temperatures at 75 mA/g active material.

approximately 100 mAh/g were obtained by cycling over a narrow window of 50–225 mV.

Fig. 6 shows the rate sensitivity for Mg_2Si cycled over 25–650 mV versus Li. Cycling at faster rates increased the number of cycles required to reach the maximum discharge capacities. Cycling at 75 mA/g instead of 15 mA/g reduced the maximum discharge capacity by nearly 40%, but capacity fading was reduced with faster rates. The anodic DCPs for the cycles with the maximum discharge capacities for each rate are shown in Fig. 7. The increase in potentials with increasing rate at the start of the discharge steps revealed significant concentration gradients within the particles at the end of the insertion steps. We are unaware of lithium diffusivity measurements in Mg_2Si near ambient temperatures. However, reducing the Mg_2Si particle size, either by synthesizing smaller particles or by mechanically removing large particles, would reduce the required diffusion distances and improve the rate capability.

The influence of temperature on the cycle lives of Mg_2Si electrodes, cycled between 25 and 650 mV versus Li at 75 mA/g, is shown in Fig. 8. Maximum discharge capacities were reached on the 1st, 2nd, and 13th cycles for cell temperatures of 60, 40, and 20 °C, respectively. The anodic DCPs for the cycles with the maximum discharge capacities are shown in Fig. 9. Peak positions for the 60 °C discharge were approximately 40 mV lower than the peak positions for the 20 °C discharge. As with the electrodes cycled at different rates, the large differences in maximum discharge capacities were attributed to being closer to equilibrium potentials at the end of the insertion steps at higher temperatures. The increase in capacity fade rate with temperature may have been due to corrosion in the electrolyte and increased particle fracturing with increased utilization.

3.3. Structural changes during cycling

XRD patterns for electrodes at various states of charge during the first are shown in Fig. 10. The electrodes were cycled over a range of 25–650 mV versus Li at 15 mA/g. Kapton tape, which was used to protect the electrodes from air exposure, was the source of the increased background below 30°. The peaks at 43.4 and 50.4° were from the copper current collectors and were used as reference peaks. For the fresh electrode, we observed the following peaks for the cubic Mg_2Si structure (space group (2 2 5)): (1 1 1) at 24.4°, (2 0 0) at 28.3°, (2 2 0) at 40.2°, (3 1 1) at 47.6°, and (4 0 0) at 58.2°.

With insertion to 25 mV, the strong Mg_2Si peaks were shifted to lower angles, and three new peaks between 30 and 40° appeared. The peak shifts and appearance of the new peaks were consistent with the formation of the Li_2MgSi phase described by Wengert et al. with a slightly larger unit cell than Mg_2Si. The new peaks at 31.3 and 36.1° were for

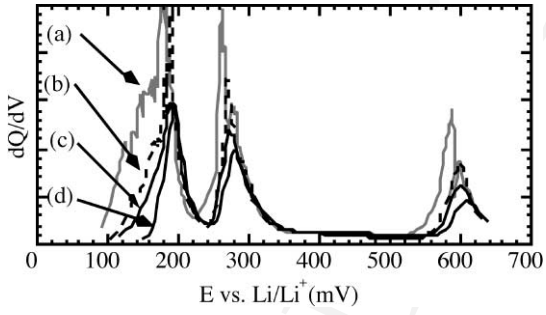

Fig. 7. Anodic DCPs (25–650 mV): (a) 2nd cycle at 15 mA/g; (b) 2nd cycle at 25 mA/g; (c) 3rd cycle at 50 mA/g and (d) 13th cycle at 75 mA/g.

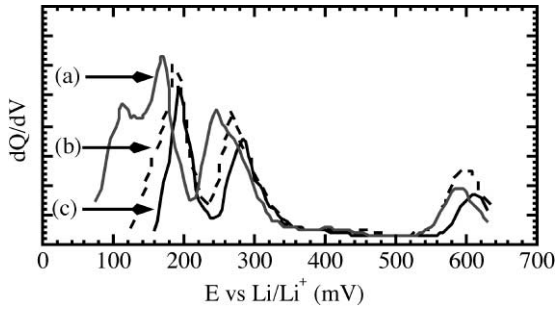

Fig. 9. Anodic DCPs (25–650 mV, 75 mA/g): (a) 1st cycle at 60 °C; (b) 2nd cycle at 40 °C and (c) 13th cycle at 20 °C.

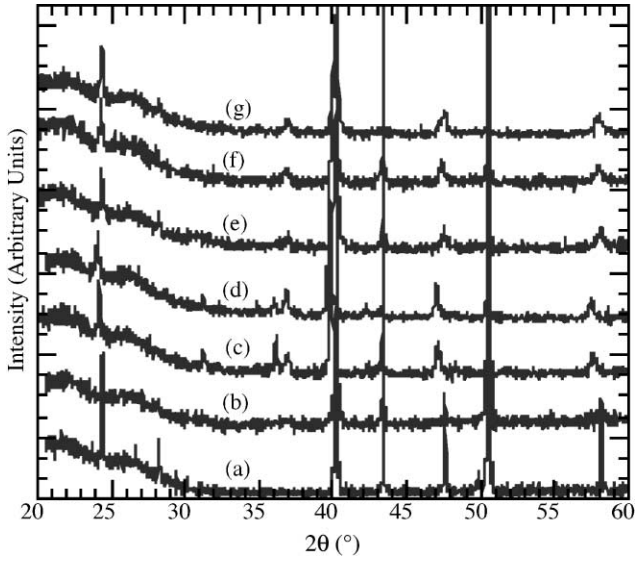

Fig. 10. XRD at various states of charge during the first cycle of Mg_2Si: (a) fresh electrode; (b) inserted to 50 mV; (c) inserted to 25 mV; (d) discharged to 150 mV; (e) discharged to 225 mV; (f) discharged to 325 mV and (g) discharged to 700 mV.

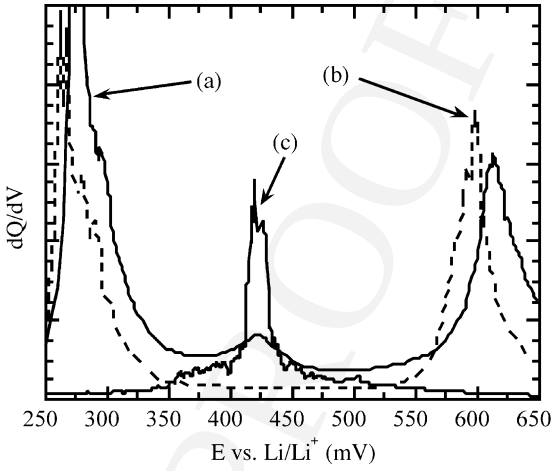

Fig. 11. Anodic DCPs: (a) Mg_2Si cycled over 5–650 mV; (b) Mg_2Si cycled over 100–650 mV and (c) Si electrode.

(3 1 1) and (5 1 1) planes for Li_2MgSi. A new peak was also observed at 37.0°. This is the location of the Mg (1 0 1) peak, which is the strongest line in the Mg pattern. Since magnesium needs to be discharged from the Mg_2Si cell to form Li_2MgSi, we would expect to observe these coexisting phases in the diffraction pattern.

After the electrode was discharged to 225 mV, the (3 1 1) and (5 1 1) peaks for Li_2MgSi disappeared and the other peaks shifted back to higher angles. This indicated that the cell slightly contracted and that Mg_2Si had been reformed. Since the (1 0 1) Mg peak remained for the rest of the discharge, the reaction to reform Mg_2Si did not proceed to completion. At the end of the first cycle, the Mg_2Si peaks were significantly broadened compared to the starting material.

After the electrode was discharged to 700 mV, the Mg_2Si peaks shifted to angles approximately 0.1° larger than the Mg_2Si peaks after the 325 mV discharge. The peak positions were identical for the electrode discharged to 700 mV and the fresh electrode. This was consistent with cell contraction after deintercalation of lithium from the Mg_2Si structure.

No evidence of binary Li–Si phases was present in the XRD patterns at various states of charge. However, reconstitution reactions in the Li–Si system at ambient temperature are kinetically limited and described as having reached "equilibrium in the lithium atom sub-lattice, but not in the silicon sub-lattice [7]". Consequently, detection of electrochemically formed Li–Si phases at ambient temperature by XRD may be difficult.

We cycled a silicon electrode between 5 and 1000 mV versus Li at 15 mA/g. The anodic DCPs is shown for this electrode in Fig. 11 along with those for Mg_2Si electrodes cycled between 5 and 650 mV and, between 100 and 650 mV. The DCPs for the electrode charged to 5 mV had a peak in the same potential range as the silicon electrode, whereas the electrode charged to 100 mV did not show any capacity in the 420 mV region. We have found the peaks in the Si potential region to be stronger for electrodes charged to lower cathodic cut-off potentials and at lower current densities.

We believe the following processes occur during lithium insertion into Mg_2Si. First, lithium is intercalated into Mg_2Si. This was indicated by observing the Mg_2Si peak shift in the XRD pattern from discharging the electrode to 700 mV. Calculating the lithium intercalation limit from our cycling data was not possible because particle utilization was incomplete in our experiments. Next, Li_2MgSi is formed and Mg is discharged from the Mg_2Si unit cell as more lithium is inserted. This was indicated by the phase change from Li_2MgSi to Mg_2Si after discharging to 225 mV. The Mg discharged in this step is also available for lithium insertion. Finally, extensive insertion to low potentials at low rates can convert Li_2MgSi into binary Li–Mg and Li–Si alloys.

4. Conclusions

Mg_2Si was successfully synthesized by mechanical alloying followed by a brief heat treatment at 600 °C. Changes in the diffraction patterns during milling indicate that silicon is the host phase for alloy formation.

Cycling stability is strongly influenced by the galvanostatic voltage limits, current densities, and cell temperatures. A maximum discharge capacity of 830 mAh/g was obtained over a wide voltage window of 5–650 mV versus Li, but the capacity fade was rapid. Discharge capacities of approximately 100 mAh/g were stable for 25 cycles over a narrow voltage window of 50–225 mV versus Li. Mass transfer limitations were apparent from the potentials that increased at the start of the discharge steps with increased current densities and decreased temperatures.

XRD experiments support the formation of Li_2MgSi. Electrochemical results indicate that Li–Si phases were formed by extensive charging at low current densities. Consequently, the Li_2MgSi structure must be converted to binary lithium alloys to accommodate additional lithium. The presence of magnesium XRD peaks at the end of the first cycle indicates that the reaction to reform Mg_2Si from Li_2MgSi was incomplete.

Acknowledgements

This work was supported by the Assistant Secretary for Energy Efficiency and Renewable Energy, Office of Transportation Technologies, Office of Advanced Automotive Technologies of the US Department of Energy under contract no. DE-AC01-76SF00098.

References

[1] R.A. Huggins, J. Power Sources 81/82 (1999) 13.
[2] H. Kim, J. Choi, H. Sohn, T. Kang, J. Electrochem. Soc. 146 (1999) 4401.
[3] T. Moriga, K. Watanabe, D. Tsuji, S. Massaki, I. Nakabayashi, J. Solid State Chem. 153 (2000) 386.
[4] A. Anani, R.A. Huggins, J. Power Sources 38 (1992) 363.
[5] S. Wengert, R. Nesper, W. Andreoni, M. Parrinello, Phys. Rev. Lett. 77 (1996) 5083.
[6] X. Niu, L. Lu, Adv. Perform. Mater. 3 (1997) 275.
[7] W.J. Weydanz, M. Wohlfahrt-Mehrens, R.A. Huggins, J. Power Sources 81/82 (1999) 237.